

ZZ PRODUCTION AT $\sqrt{s} = 13$ TeV IN FOUR-LEPTON
EVENTS USING THE CMS DETECTOR AT THE CERN
LHC

by

Nathaniel Woods

A dissertation submitted in partial fulfillment of
the requirements for the degree of

Doctor of Philosophy
(Physics)

at the
UNIVERSITY OF WISCONSIN – MADISON
2017

Defended on X August 2017

Dissertation approved by the following members of the Final Oral Committee:

Wesley Smith · Bjorn Wiik Professor of Physics
Sridhara Dasu · Professor of Physics
Matthew Herndon · Professor of Physics
Someone · Professor of Physics
Someone · Professor of Something

Abstract

This thesis presents some cool stuff.

Acknowledgements

Nice people are nice.

Contents

Abstract	i
Acknowledgements	ii
List of Figures	viii
List of Tables	ix
1 The Standard Model	1
1.1 Introduction	1
1.2 Matter and Force	1
1.3 Electroweak Symmetry Breaking and the Higgs Boson	1
1.4 Proton-Proton Collisions	2
1.5 Diboson Physics	2
1.5.1 Vector Boson Scattering	2
1.6 Limitations and Possible Extensions	2
1.6.1 Anomalous Gauge Couplings	2
1.7 Topics Covered In This Thesis	2
2 ZZ Phenomenology and Previous Results	3
2.1 Nonresonant ZZ/Z γ^* Production and Decay	3
2.1.1 Nonresonant Z γ^* Production	3

2.1.2	Vector Boson Scattering	3
2.1.3	Prior Measurements	3
2.2	Resonant $ZZ^*/Z\gamma^*$ Production	4
2.2.1	Z Boson Decays to Four Leptons	4
2.2.2	Higgs Boson Production	4
2.2.3	Prior Measurements	4
2.3	Anomalous Gauge Couplings	4
2.3.1	Previous Limits	4
2.4	Background Processes	4
3	The CMS Experiment and the CERN LHC	5
3.1	The CERN Large Hadron Collider	6
3.1.1	Accelerator Chain, Layout, and Detectors	7
3.1.2	Operating Parameters	10
3.1.2.1	Design	11
3.1.2.2	Run I	12
3.1.2.3	Run II	13
3.2	The Compact Muon Solenoid Detector	14
3.2.1	Terminology and Geometry	15
3.2.2	Magnet and Inner Tracking System	16
3.2.2.1	Pixel Detector	18
3.2.2.2	Strip Tracker	19
3.2.3	Electromagnetic Calorimeter	20
3.2.4	Hadronic Calorimeter	21
3.2.5	Muon Spectrometer	24
3.2.5.1	Drift Tubes	24

3.2.5.2	Cathode Strip Chambers	26
3.2.5.3	Resistive Plate Chambers	27
3.2.6	Data Acquisition and Trigger	28
3.2.6.1	Level-1 Trigger	28
3.2.6.2	High-Level Trigger	31
3.2.7	Luminosity Determination	32
4	Simulation	34
4.1	Monte Carlo Event Generation	34
4.1.1	Matrix Element Generation	34
4.1.2	Parton Shower, Hadronization, and Underlying Event	34
4.1.3	Pileup Simulation	34
4.2	Detector Simulation	34
5	Object Reconstruction and Selection	35
5.1	Track Reconstruction and Vertex Identification	35
5.2	Particle Flow Reconstruction	35
5.2.1	PF Candidates	35
5.2.1.1	Muons	35
5.2.1.2	Electrons and Charged Hadrons	36
5.2.1.3	Photons and Neutral Hadrons	36
5.2.2	Jets	36
5.2.3	Missing Transverse Energy	36
5.3	Object Identification and Selection	36
5.3.1	Electrons	36
5.3.2	Muons	36
5.3.3	Jets	36

5.3.4	Final State Photon Radiation	37
5.3.5	Misidentified Objects	37
5.4	ZZ Candidate and Event Selection	37
5.4.1	Z Candidate Selection	37
5.4.2	ZZ Candidate Selection	37
5.4.3	Background Estimation	37
5.4.4	VBS Signal Selection	37
6	Analysis Strategy	38
6.1	Background Estimation	38
6.2	Systematic Uncertainties	41
6.3	Fiducial and Total Cross Section Calculation	42
6.3.1	Signal Strength Extraction	44
6.3.2	Total ZZ Cross Section and $Z \rightarrow 4\ell$ Branching Fraction	44
6.4	Differential Cross Sections	45
6.4.1	Unfolding	46
6.4.2	Uncertainties	47
6.5	VBS Signal Extraction	48
6.6	Anomalous Gauge Coupling Searches	49
7	Results	50
7.1	Four-Lepton Yield and Distributions	50
7.1.1	Full Spectrum	50
7.1.2	$Z \rightarrow 4\ell$ Resonance	50
7.1.3	Higgs Resonance	50
7.1.4	ZZ Production	50
7.2	ZZ Fiducial and Total Cross Section	51

7.2.1	$Z \rightarrow 4\ell$ Branching Fraction	51
7.3	Differential Cross Sections	51
7.4	Vector Boson Scattering	51
7.5	Anomalous Coupling Limits	51
8	Conclusions	52
8.1	Summary	52
8.2	Outlook	52
Bibliography		53

List of Figures

3.1	LHC dipole schematic	8
3.2	LHC accelerator and experiment layout	9
3.3	Integrated luminosity delivered to CMS in each LHC run period . .	13
3.4	CMS cutout schematic	15
3.5	Inner tracker layout	18
3.6	Tracker material budget in radiation lengths	19
3.7	ECAL geometry	20
3.8	HCAL geometry	23
3.9	Total material budget in nuclear interaction lengths	23
3.10	Muon system geometry	25
3.11	Trigger data flow	31
6.1	Misidentification rates for electrons and muons	40

List of Tables

3.1 LHC beam parameters	12
6.1 Systematic uncertainties on the total yield	43

Chapter 1

The Standard Model

1.1 Introduction

Some history and stuff

1.2 Matter and Force

Does this need subsections? Not the way it's structured in my head right now, but maybe it could have one subsection for fermions and another for gauge bosons.

1.3 Electroweak Symmetry Breaking and the Higgs Boson

Everybody's favorite fundamental scalar boson

1.4 Proton-Proton Collisions

Bang

1.5 Diboson Physics

Really only ZZ, but you get the point

1.5.1 Vector Boson Scattering

Scatter scatter

1.6 Limitations and Possible Extensions

It misses a few things

1.6.1 Anomalous Gauge Couplings

Pro tip: we won't see them

1.7 Topics Covered In This Thesis

Chapter 2

ZZ Phenomenology and Previous Results

Phenomenal!

2.1 Nonresonant ZZ/Z γ^* Production and Decay

Dibosons come, dibosons go

2.1.1 Nonresonant Z γ^* Production

Virtual particles. Spoooooooooky!

2.1.2 Vector Boson Scattering

Them jets tho

2.1.3 Prior Measurements

The literature before I got here

2.2 Resonant $ZZ^*/Z\gamma^*$ Production

This resonates with me

2.2.1 Z Boson Decays to Four Leptons

Prior measurements of this probably don't need their own subsubsection

2.2.2 Higgs Boson Production

2.2.3 Prior Measurements

Discovery!

2.3 Anomalous Gauge Couplings

Triple and quartic

2.3.1 Previous Limits

Pro tip: they aren't there

2.4 Background Processes

Basically, $Z+jets$ and $t\bar{t}$

Chapter 3

The CMS Experiment and the CERN LHC

Production of controlled high-energy particle collisions, and detection of the decay products resulting from those collisions, are monumental technical challenges. The apparatus used to obtain the results presented in this thesis are the result of decades of work by thousands of scientists and engineers, making use of many techniques developed in the course of building and operating previous experiments. The CERN Large Hadron Collider (LHC) [1, 2] accelerates pairs of charged hadron (proton or lead ion) beams to high energies and collides them to provide a source of data to several fully independent detectors, including the Compact Muon Solenoid (CMS) [3], which collected the data used in the studies presented here. Detailed descriptions of the LHC and CMS follow.

3.1 The CERN Large Hadron Collider

The LHC, the most powerful particle accelerator and collider ever built, is a 26.7 km circumference ring of superconducting magnets running through tunnels roughly 100 m below the suburbs and countryside near Geneva, Switzerland. It first produced collisions suitable for collecting physics data in 2010 before generating large datasets with beam energies of 3.5 TeV in 2011 and 4 TeV in 2012. Following a shutdown for upgrades and repairs, it returned in 2015 and 2016 to deliver beam energies of 6.5 TeV. Beams collide head-on so that the center-of-mass frame of the proton-proton system is the rest frame of the detectors, giving proton-proton center-of-mass energies of 7, 8, and 13 TeV respectively for collisions in 2010–2011, 2012, and 2015–2016. Each successive energy was the highest ever achieved in controlled proton-proton collisions, giving unprecedented access to extremely high-energy processes at every step.

In addition to increasing collision energies, the LHC increased its rate of collisions with each new machine configuration. The average event rate dN/dt for a process with production cross section σ is determined by the instantaneous luminosity \mathcal{L} of the collider,

$$\frac{dN}{dt} = \mathcal{L}\sigma \quad (3.1)$$

so a high instantaneous luminosity is vital to the timely observation of rare processes like Higgs boson production. The LHC’s unprecedented luminosities have allowed collection of the largest physics datasets in history.

The desire for high luminosities drove the decision to collide protons with other protons instead of with antiprotons as was done at Tevatron, LHC’s predecessor at Fermilab in Batavia, IL. Antiprotons simply cannot be produced in sufficient quantities for a collider on this scale. Many of the physics processes Tevatron was designed to study are $q\bar{q}$ -initiated, so it is useful to have valence antiquarks available in

the collisions. The LHC was designed with Higgs boson production in mind, and the two most important Higgs production modes are proton/antiproton agnostic. Even for $q\bar{q}$ -initiated processes, valence antiquarks are less critical at the LHC because, for equal parton momenta, protons have larger antiquark content at LHC energies than at Tevatron energies (1.98 TeV center-of-mass energy) as discussed in Section 1.4.

In addition to protons, the LHC can accelerate beams of lead nuclei to 2.51 TeV per nucleon, also the highest ever achieved. All studies presented in this thesis were performed on proton-proton collision data, rendering the details of so-called “heavy ion” beams beyond the scope of this document.

Beams are maintained and manipulated with magnets, most of them made of superconducting niobium-titanium (NbTi) winding cooled to 1.9 K by superfluid helium. Dipole magnets with fields up to 8.33 T bend the beam around the ring, interspersed with quadrupoles for focusing. More quadrupoles and higher-moment magnets keep the beams focused, squeeze them for collisions, and apply a number of corrections. Superconducting radio frequency (RF) cavities operating at 400 MHz accelerate the beam, maintain it at its final energy, and maintain bunch shape and spacing.

3.1.1 Accelerator Chain, Layout, and Detectors

The LHC was built in tunnels originally constructed for the Large Electron-Positron Collider (LEP), an e^+e^- collider that operated from 1989 to 2000. Using existing caverns, tunnels, and infrastructure was a substantial cost-saving measure, but imposed several important constraints on the LHC’s design. In LEP, the electron and positron beams could be accelerated in opposite directions by the same magnets, because they are oppositely charged. Conversely, proton beams require opposite magnetic fields for the two beams. Because the tunnels were not wide enough to accommodate two completely separate beam lines, most of the magnets in the LHC use a twin-bore design,

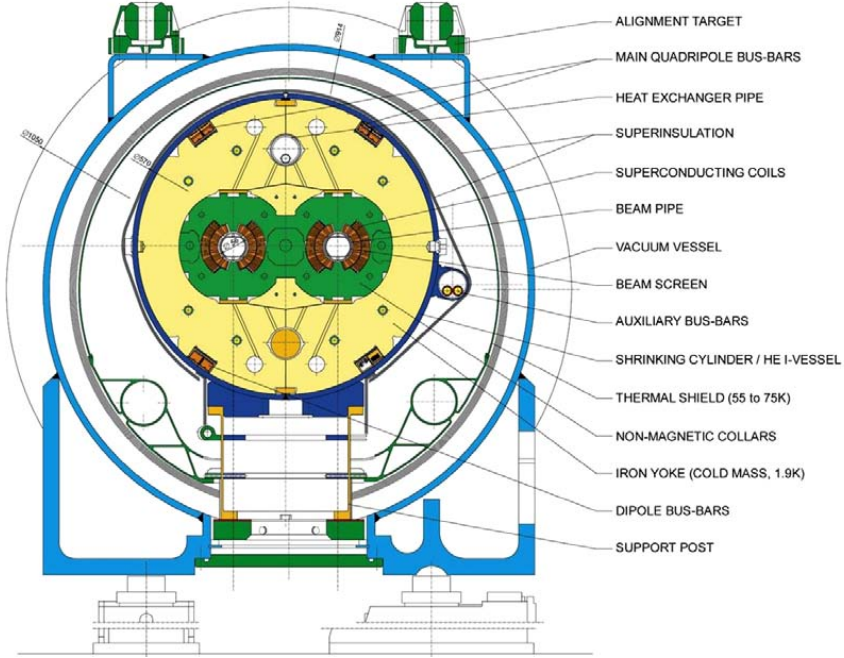


Figure 3.1: Schematic cross section of an LHC dipole and its attendant electrical and cryogenic infrastructure, reproduced from Ref. [1].

shown schematically in Fig. 3.1, in which the pipes and windings for the two beams share a common cryogenic system. The electromagnetic, mechanical, and cryogenic coupling of the two beamlines represents a significant engineering challenge.

Because no single accelerator has the dynamic range necessary to take a stationary proton to TeV-scale energies, a chain of smaller accelerators repurposed from previous experiments feeds moderate-energy protons into LHC. Protons are obtained by ionizing hydrogen atoms, then accelerated to 50 MeV by the Linac 2 linear accelerator and injected into the Proton Synchrotron Booster (PSB), the first of several circular accelerators. The PSB feeds 1.4 GeV protons into the Proton Synchrotron (PS), which in turn injects them into the Super Proton Synchrotron (SPS) at 26 GeV. The protons are then accelerated to 450 GeV in the SPS before being injected into LHC. A diagram of the entire accelerator chain is shown in Fig. 3.2.

The ring is divided into eight sectors, each of which features a 528 m straight

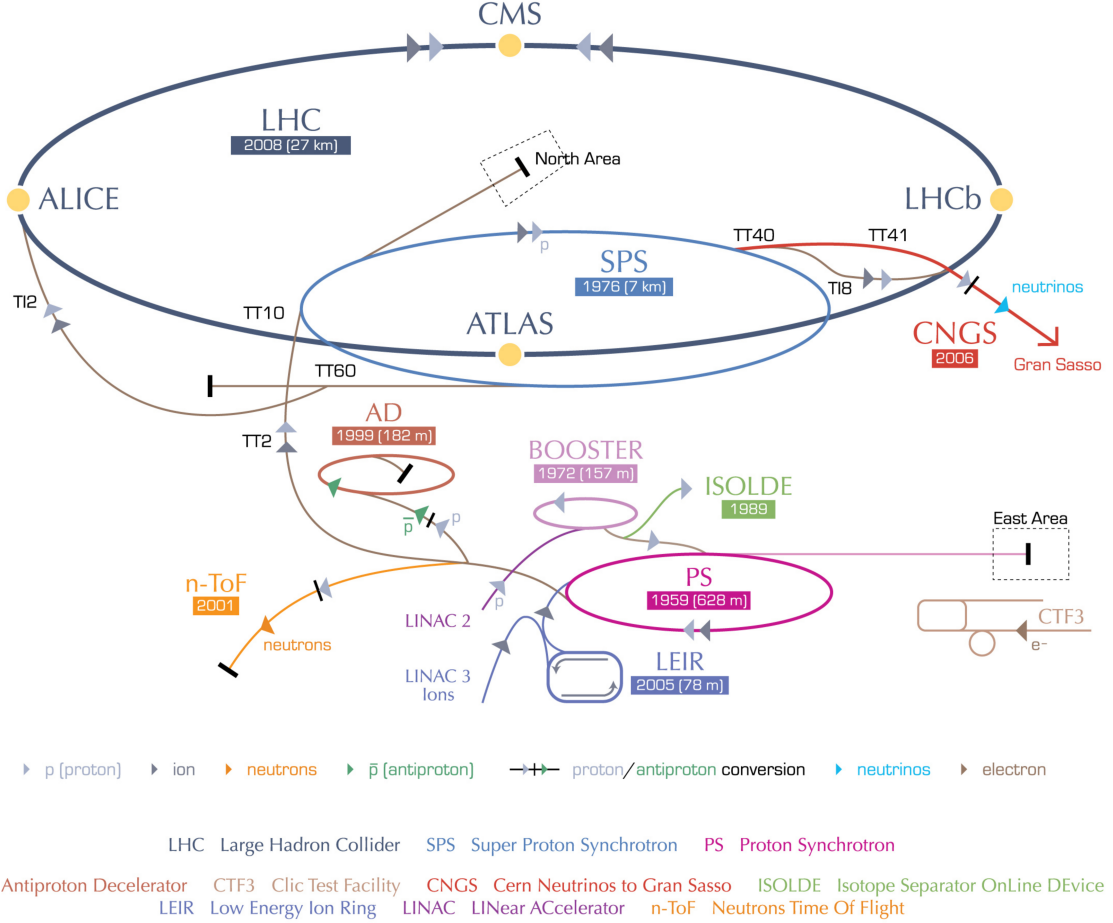


Figure 3.2: A schematic of the LHC accelerator chain and peripheral experiments, reproduced from Ref. [4].

section connected to the adjacent sections by 2.45 km arcs. The straight section length was set by the need for RF cavities to accelerate LEP beams to counteract synchrotron radiation, which is a primary factor limiting electron and positron beam energy. This is not ideal for proton beams; protons' much higher mass means they radiate less and need fewer RF cavities. The straight sections feature “insertion” points numbered with Point 1 at the main CERN site in Meyrin, Switzerland, and the rest numbered 2–8, increasing in the clockwise direction when viewed from above. Points 1, 2, 5, and 8 have beam crossing points and host detectors to study the resulting proton-proton collisions. Points 3 and 7 feature collimators to remove nonuniformities in the beams.

The RF cavities are at Point 4 and the beams are dumped after use into absorbers at Point 6.

The CMS detector is at Point 5 in Cessy, France, the furthest point on the ring from the Meyrin site and Point 1, which houses ATLAS [5], a similar but fully independent general-purpose particle detector. CERN and the science funding agencies support CMS and ATLAS equally so that any measurement or discovery made by one can be made concurrently or verified by the other. The other two experimental insertions feature specialized detectors studying collisions at lower-luminosity beam interaction points. The LHCb detector [6], at Point 8, studies hadronic physics with an emphasis on b-mesons, and ALICE [7] studies heavy ion collisions at Point 2. Three smaller experiments share interaction points with the larger detectors, with TOTEM [8] studying proton structure and the total proton-proton interaction cross section next to CMS; LHCf [9] studying the π^0 energy spectrum and multiplicity near ATLAS; and MoEDAL [10] searching for magnetic monopoles or other heavy, stable, ionizing particles at Point 8 with LHCb.

3.1.2 Operating Parameters

With the beam energy set by the radius of the ring and the strength of available magnets, the number of interesting physics events produced in LHC collisions depends only on the integrated luminosity

$$\mathcal{L}_{int} = \int \mathcal{L} dt, \quad (3.2)$$

where \mathcal{L} is the instantaneous luminosity defined in Eq. 3.1 and the integral runs over the time the machine spends in collisions mode. LHC's availability for collisions depends on the electrical and mechanical stability of the accelerators and their support systems, including the cryogenics and the vacuum in the beam pipe. The

instantaneous luminosity while running depends only on the beam parameters. For symmetric beams which each have n_b colliding gaussian bunches of intensity (i.e. number of protons in the bunch) N_b , orbiting the ring with frequency f_{rev} and relativistic factor $\gamma = E_p/m_p$, the instantaneous luminosity is give by

$$\mathcal{L} = f_{rev} \frac{n_b N_b^2 \gamma}{4\pi \beta^* \epsilon_N} R, \quad (3.3)$$

where β^* is the amplitude of the beams' betatron oscillations around the nominal ring path at the interaction point, the normalized emittance ϵ_N is a measure of the beams' spread in both position and momentum space, and R is a geometrical factor accounting for the beam crossing angle,

$$R = \sqrt{1 + \left(\frac{\theta_c \sigma_z}{2\sigma^*} \right)^2}. \quad (3.4)$$

Here θ_c is the beams' crossing angle, and σ_z and σ^* are respectively the longitudinal and transverse RMS widths of the bunches in the lab frame.

3.1.2.1 Design

The machine parameters in the LHC design specification can be seen in the first column of Table 3.1. Many of the design parameters, in particular the energy and number of colliding bunches, have not been met due to a failure during initial testing in September 2008. A fault in a superconducting bus bar connection between a dipole and a quadrupole caused an electrical arc which ruptured the cryostat, leading to a rapid and destructive release of helium gas [11]. When LHC was brought back online in 2010 after repairs and upgrades intended to prevent similar incidents in the future, its operating parameters were changed to further reduce the risk of catastrophic failure. Some luminosity-related parameters were adjusted to mitigate the resulting loss of physics discovery potential as much as possible. Further upgrades have improved

Table 3.1: LHC beam parameters as designed and in practice. As stated in the text, n_b is the number of colliding bunches, N_b is the number of protons in each bunch, β^* is the betatron amplitude at the interaction point, ϵ_N is the normalized emittance, and $\mathcal{L}_{(int)}$ is the instantaneous (integrated) luminosity.

Year	Design		Run I		Run II	
		2010	2011	2012	2015	2016
Energy per beam (TeV)	7	3.5	3.5	4	6.5	6.5
Bunch spacing (ns)	25	150	50	50	25	25
n_b	2808	348	1331	1368	2232	2208
$N_b (10^{11})$	1.15	1.2	1.5	1.7	1.15	1.25
β^* (m)	0.55	3.5	1.0	0.6	0.8	0.4
ϵ_N (mm mrad)	3.75	2.2	2.3	2.5	3.5	3.0
Peak pileup	FIXME	4	17	37	22	49
Peak $\mathcal{L} (10^{34} \text{cm}^{-2}\text{s}^{-1})$	1	0.02	0.35	0.77	0.52	1.53
$\mathcal{L}_{int} (\text{fb}^{-1})$		0.04	6.1	23.3	4.2	41.1

machine performance, with some parameters now meeting or exceeding the design specification.

3.1.2.2 Run I

The LHC was brought back online in 2010 at half its design energy, with 3.5 TeV beam energy, which was increased to 4 TeV in 2012. The bunch intensity was also lower, with bunches spaced 50 ns apart instead of 25 ns. The longer bunch spacing was chosen to allow full exploitation of excellent injection chain performance [12]. Beams exiting the SPS had bunch intensity as much as 50% higher than anticipated in the original LHC design and beam emittance as low as 67% of nominal. This allowed the LHC to achieve 77% of its design instantaneous luminosity in 2012 despite having roughly half as many bunches in each beam.

Machine availability was overall good considering the complexity and relative newness of the LHC, with about 36% of scheduled time spent in stable beams. In all, LHC delivered 6.1fb^{-1} to CMS and ATLAS in 2011 and 23.3fb^{-1} in 2012, enough to

allow discovery of the Higgs boson. The integrated luminosity for each year of LHC operation is shown as a function of calendar month and day in Fig. 3.3.

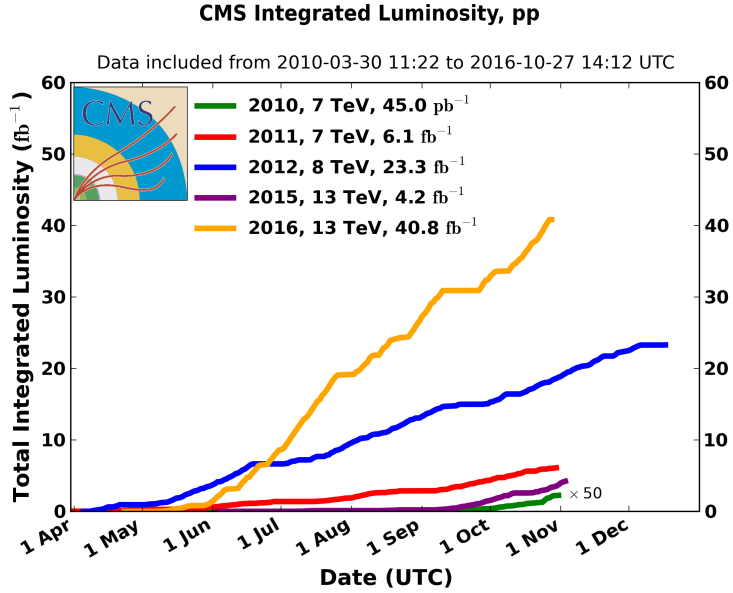


Figure 3.3: The integrated luminosity delivered to CMS in each year of LHC operation, shown as a function of the date within the year.

3.1.2.3 Run II

The LHC shut down for 2013 and 2014 to allow a number of repairs and upgrades, including measurements, repairs and upgrades on the electrical connections and cryogenic safety systems like the ones that failed in 2008. Beam energies could then be increased to 6.5 TeV, close to the nominal 7 TeV. The bunch spacing was decreased to 25 ns while maintaining low emittance and high bunch intensity with the implementation of the beam compression merging and splitting (BCMS) scheme in which bunches are merged in the PS before they are split for injection into SPS, allowing higher bunch intensity [13]. This was offset by vacuum problems in the SPS beam dump, which limited the total number of colliding bunches to around 2200 [14]. Improvements in collimators and beam optics reduced β^* to 40 cm in 2016, lower than

the design β^* of 55 cm. Overall instantaneous luminosities were substantially higher than originally designed.

Machine availability in Run II was excellent, with over 60% of planned time spent in stable beams [14]. Mechanical problems kept LHC out of commission for much of 2015, and only 4.2 fb^{-1} were delivered to Points 1 and 5, but the integrated luminosity in 2016, 41.1 fb^{-1} , was far above the roughly 25 fb^{-1} expected and more than all previous runs combined.

3.2 The Compact Muon Solenoid Detector

The CMS detector [3] is a general-purpose particle detector located in a cavern roughly 100 m below LHC Point 5. Though designed to do a wide range of physics analyses, CMS was designed specifically with Higgs boson discovery in mind. Primary design goals include

- High-efficiency reconstruction of charged particles with precise measurement of their trajectories and momenta
- Good electromagnetic energy resolution, including diphoton and dielectron mass resolution
- Hermetic calorimetry for good missing transverse energy and dijet mass resolution
- Good muon identification, momentum resolution (including dimuon mass resolution), and charge determination over a broad range of energies

To this end, CMS features a silicon tracker, a scintillating crystal electromagnetic calorimeter (ECAL), and a hermetic hadronic calorimeter (HCAL) inside a 3.8 T

solenoid magnet surrounded by ionized gas muon tracking devices, all of which can be seen as part of the whole detector in Fig. 3.4. Decisions on which events to read out are made on-line by a two-level trigger system. Descriptions of these systems follow.

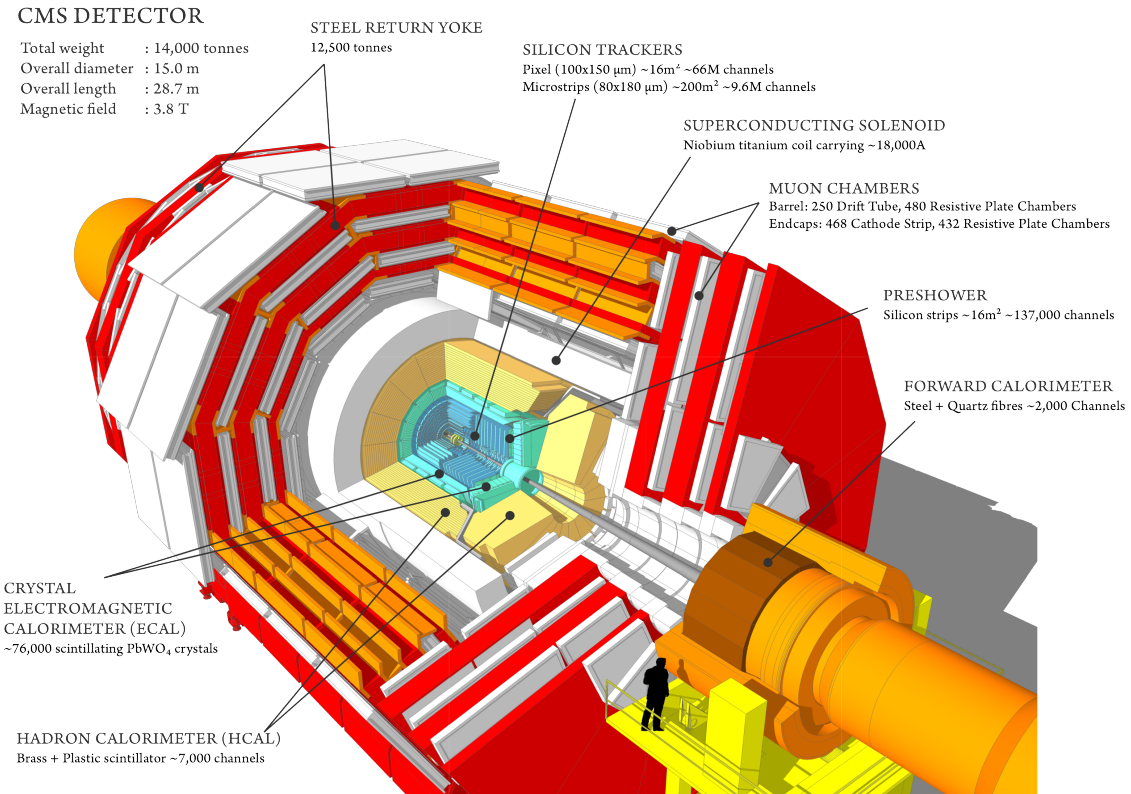


Figure 3.4: Cutout schematic of CMS with all major subdetectors, the beamline, the magnet, and the return yoke visible. Reproduced from Ref. [15].

3.2.1 Terminology and Geometry

The CMS detector systems are arranged in cylindrical layers with the interaction point at the center, serving as the origin for the coordinate system. The coordinate system is defined with the positive- x direction pointing toward the center of the ring, positive- y pointing vertically up, and positive- z pointing parallel to the beam

in the counterclockwise direction when the LHC ring is viewed from above. Particle momenta are typically expressed in quasicylindrical coordinates (p_T, η, ϕ) . Here p_T is the magnitude of the particle's momentum transverse to the beam

$$p_T \equiv \sqrt{p_x^2 + p_y^2}, \quad (3.5)$$

and ϕ is the azimuthal angle, i.e. the angle from the x -axis to the particle's trajectory in the x - y plane. The pseudorapidity η is defined as

$$\eta \equiv -\ln \left[\tan \left(\frac{\theta}{2} \right) \right] \quad (3.6)$$

where θ is the polar angle measured from the z -axis. The relativistic rapidity

$$y \equiv \frac{1}{2} \ln \left(\frac{E + p_z}{E - p_z} \right), \quad (3.7)$$

converges to the pseudorapidity in the limit of massless particles. Pseudorapidity is preferred to rapidity because it is purely geometrical, with no dependence on the particle energy. Both are preferred over θ because rapidity differences are invariant under longitudinal boosts, and because hadron flux at colliders is roughly constant as a function of rapidity. The transverse energy E_T is the the magnitude of the particle's four-momentum transverse to the beam, equal to p_T in the limit of massless particles. Spatial coordinates are expressed as (r, η, ϕ) , where r is the distance from the beam in the x - y plane.

3.2.2 Magnet and Inner Tracking System

A particle of charge q moving through a uniform magnetic field of strength B that points in the z direction will travel in a helix of radius R , given by

$$R = \frac{p_T}{|q|B}, \quad (3.8)$$

with the chirality of the helix determined by the sign of q . Thus one can determine the transverse momentum of the particle by measuring its path through the magnetic field and finding the radius of curvature. In practice, all but the lowest-energy particles leave too short an arc in the detector for direct measurement of the radius, so the sagitta of the arc is used instead, given by

$$s = \frac{qBL^2}{8p_T} \quad (3.9)$$

where L is the length of the chord spanning the arc (typically equal to the radius of the tracking system). The transverse momentum resolution varies as

$$\frac{\delta p_T}{p_T} \propto \frac{p_T}{BL^2}, \quad (3.10)$$

so a strong field and a large tracking volume are vital to keeping measurements precise even at high energies.

To this end, CMS contains the world's largest superconducting magnet¹, a solenoid 13 m long and 6 m in diameter, which generates a nearly-uniform 3.8 T field in the centralmost part of the detector. To measure the paths of charged particles in the field, the volume closest to the interaction point contains layers of silicon sensors that detect hits from charged particles with high efficiency and excellent position resolution, between 4.4 cm and 1.1 m from the beam for 2.7 m on either side of the interaction point. This system, called the inner tracker and shown schematically in Fig. 3.5, consists of an inner pixel detector surrounded by a larger silicon strip detector. Both consist of concentric cylinders of sensors covering the barrel of the detector capped by discs covering the high- η region, up to $|\eta| < 2.5$. With a total of roughly 200 m² of silicon, the inner tracker is the largest silicon tracker in the world. Tracks may be reconstructed with hits in as many as 14 layers. The downside

¹Largest in the sense of having the largest stored energy when at constant full field. The largest by size is the ATLAS barrel toroid.

of this is that the tracker represents a substantial amount of material for electrons and photons to interact with before they reach the calorimeters, with total material budget between 0.4 radiation lengths ($\eta = 0$) and 1.8 radiation lengths ($|\eta| \approx 1.4$), as shown. The tracker-only p_T uncertainty is around 1.2% at 200 GeV and 15% at 1 TeV. Tracker readout is too slow for it to be used in the L1 trigger (see Section 3.2.6.1), so the other systems must be used for this purpose.

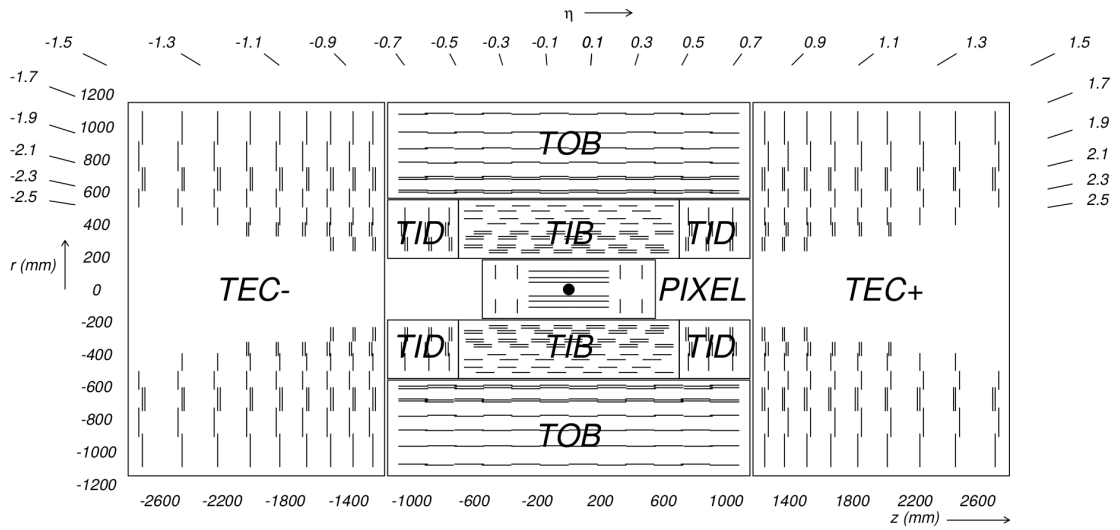


Figure 3.5: Diagram of the inner tracker layout, reproduced from Ref. [3].

3.2.2.1 Pixel Detector

The pixel detector, consisting of three layers in the barrel and two in the endcap, is responsible for accurate reconstruction of primary proton-proton interaction vertices and secondary vertices from b-meson decays, as well as providing “seed” tracks that may be used in strip tracker reconstruction. As the system closest to the interaction point, the pixel system experiences the highest charged-particle flux must have extremely fine granularity to differentiate between nearby particles. The 66 million pixels in the system have a cell size of $100 \times 150 \mu\text{m}^2$. Interpolation of the analog signals from the individual pixels allows a final spatial resolution of $15 \mu\text{m}$ in each

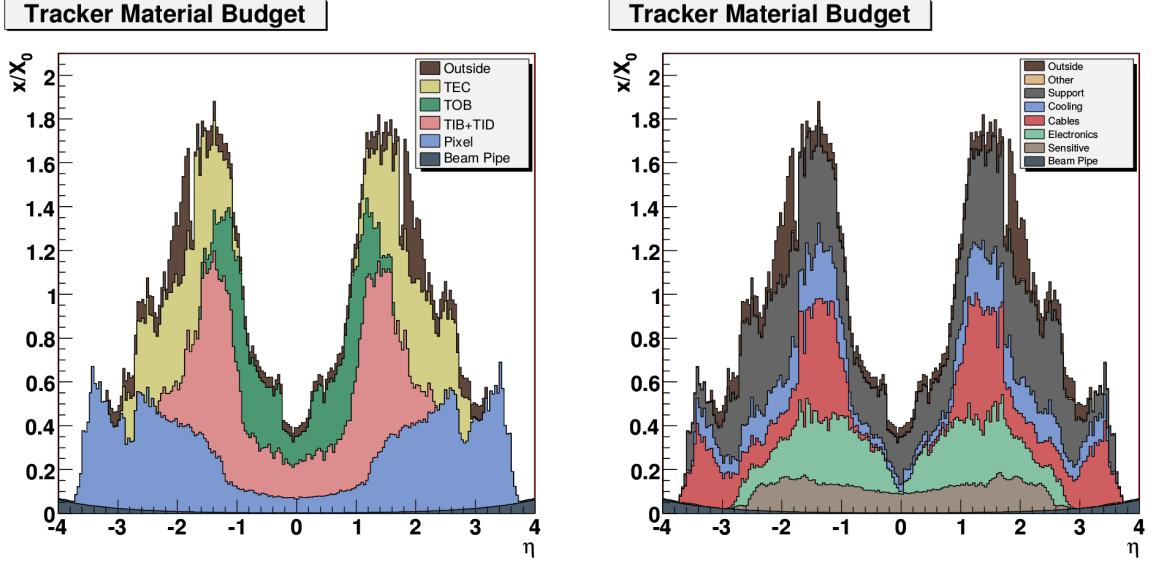


Figure 3.6: Total tracker material budget in units of electromagnetic radiation lengths, as a function of pseudorapidity. At (left) the total is divided by detector subsystem, at (right) by the function of the material. Reproduced from Ref. [3].

direction. The outermost barrel layer is 10.2 cm from the beam, and the second endcap disk is 46.5 cm from the interaction point. The sensor modules are arranged such that at least three sensors cover the solid angle within the pixels’ acceptance.

3.2.2.2 Strip Tracker

Outside the pixels is the silicon strip tracker, extending out to 1.1 m in the r direction and ± 2.8 m in the z direction. The tracker is divided into inner and outer subdetectors, each of which has both barrel cylinders and endcap discs. In total, there are ten layers in the barrel and nine in each of the endcaps. The inner tracker uses 320 μm -thick sensors with a typical strip cell size of $10\text{ cm} \times 80\text{ }\mu\text{m}$, leading to hit resolutions of 23–35 μm . The outer tracker uses 500 μm -thick sensors with typical strip sizes up to $25\text{ cm} \times 180\text{ }\mu\text{m}$, leading to hit resolutions of 35–53 μm .

3.2.3 Electromagnetic Calorimeter

Outside of the tracker is the electromagnetic calorimeter (ECAL), which is designed to absorb and measure the energy of electrons and photons. ECAL is made of 68,524 lead tungstate (PbWO_4) crystals arranged in a cylindrical barrel (EB) covering $|\eta| < 1.444$ and two endcap discs (EE) covering $1.566 < |\eta| < 3.0$. The geometry of the ECAL barrel and endcap can be seen in Fig. 3.7; the small gap between the barrel and endcap is necessary to accommodate cabling and support structures for the tracker. PbWO_4 crystals scintillate blue-green light and are optically transparent, so the resulting light can be read out by avalanche photodiodes (APDs) in the barrel and vacuum phototriodes (VPTs) in the endcap. ECAL's granularity is set by PbWO_4 's small Molière radius of 2.2 cm, which is also the size of the square front faces of the barrel crystals, which flare out to 2.6 cm at the back, giving them a truncated pyramid shape covering a roughly 0.0174×0.174 area of $\eta\phi$ space. The endcap crystals go from 2.86 cm squares at the front to 3.0 cm at the back.

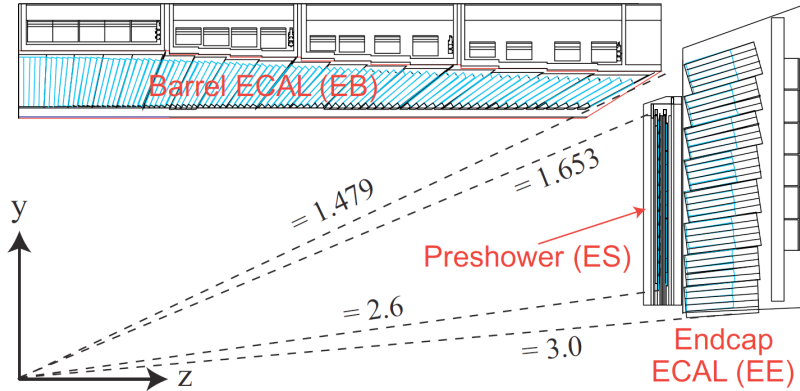


Figure 3.7: Diagram of ECAL geometry, reproduced from Ref. [16].

One of the primary design innovations of CMS—the eponymous compactness—was to place the calorimetry inside the magnet so that tracks can be unambiguously associated with energy deposits in the calorimeters without interference from

scattering in the magnet coils. This is possible in part thanks to the high density (8.28 g/cm^3) and short radiation length (0.89 cm) of PbWO_4 , which allow ECAL crystals to be only 23 cm long in the barrel and 22 cm long in the endcap while still spanning 25.8 and 24.7 radiation lengths, respectively. This is enough to ensure that essentially no electrons or photons escape ECAL with any appreciable remaining energy.

The total scintillation light yield is relatively low, averaging just 4.5 photons per MeV deposited. The Poisson fluctuations in the yield are the largest contribution to ECAL energy resolution for most electron and photon energies, represented by the first term in the full resolution equation,

$$\left(\frac{\delta E}{E}\right)^2 = \left(\frac{2.8\%}{\sqrt{E/\text{GeV}}}\right)^2 + \left(\frac{0.12}{E/\text{GeV}}\right)^2 + (0.30\%)^2. \quad (3.11)$$

The second term comes from electronic noise and noise from pileup, and the last term represents intrinsic differences between crystals. The upside to PbWO_4 's scintillation is that it is fast: roughly 80% of the light is emitted in the 25 ns between bunch crossings.

3.2.4 Hadronic Calorimeter

Between ECAL and the magnet is the hadronic calorimeter (HCAL), responsible for measuring the energy of hadronic jets. HCAL is a sampling calorimeter, meaning that the hadrons pass through dense, uninstrumented material and the products of the resulting interactions deposit energy in scintillators which are used to measure the total energy of the original incoming particles. The HCAL barrel (HB, $|\eta| < 1.305$) and endcap (HE, $1.305 < |\eta| < 3.0$) are made of layers of brass absorber interleaved

with plastic scintillating tiles. The energy resolution in HB and HE is given by

$$\left(\frac{\delta E}{E}\right)^2 = \left(\frac{90\%}{\sqrt{E/\text{GeV}}}\right)^2 + (4.5\%)^2. \quad (3.12)$$

The first term is from the stochastic evolution of hadronic showers in the absorber, the second is from calibration uncertainties.

Because HB is not enough to absorb all hadrons in the barrel, there is an extra outer HCAL component (HO) outside of the magnet, consisting of two more layers of scintillator on either side of a 20 cm-thick iron “tail catcher” covering $|\eta| < 1.3$. The geometry of HB, HE, and HO is shown in Fig. 3.8. The thickness of HB and HE is constrained by the size of the magnet, varying from 5.4 nuclear interaction lengths in the central barrel to more than 10 in the endcaps. With HO and the 1.1 interaction lengths in ECAL considered, no part of the calorimeter system spans fewer than 11.8 interaction lengths except in the gaps between barrel and endcap, minimizing the flux of hadronic “punchthrough” interacting with the muon system. The total material budget in front of the layers of the muons systems is shown in Fig. 3.9.

Closer to the beam line on each side, the forward hadronic calorimeter ($\text{HF}, 3.0 < |\eta| < 5.2$) is made of iron instead of brass to maximize radiation hardness and acts as a Cherenkov detector with quartz fibers as the active detection element. Half the fibers extend the entire depth of HF, while the other half start after the hadrons have traversed 22 cm of iron, allowing electromagnetic and hadronic energy to be differentiated without ECAL. The energy resolution in HF is given by

$$\left(\frac{\delta E}{E}\right)^2 = \left(\frac{172\%}{\sqrt{E/\text{GeV}}}\right)^2 + (9\%)^2, \quad (3.13)$$

where the terms have the same physical interpretation as those in Eq. 3.12. HF improves CMS’s missing energy resolution by roughly a factor of three.

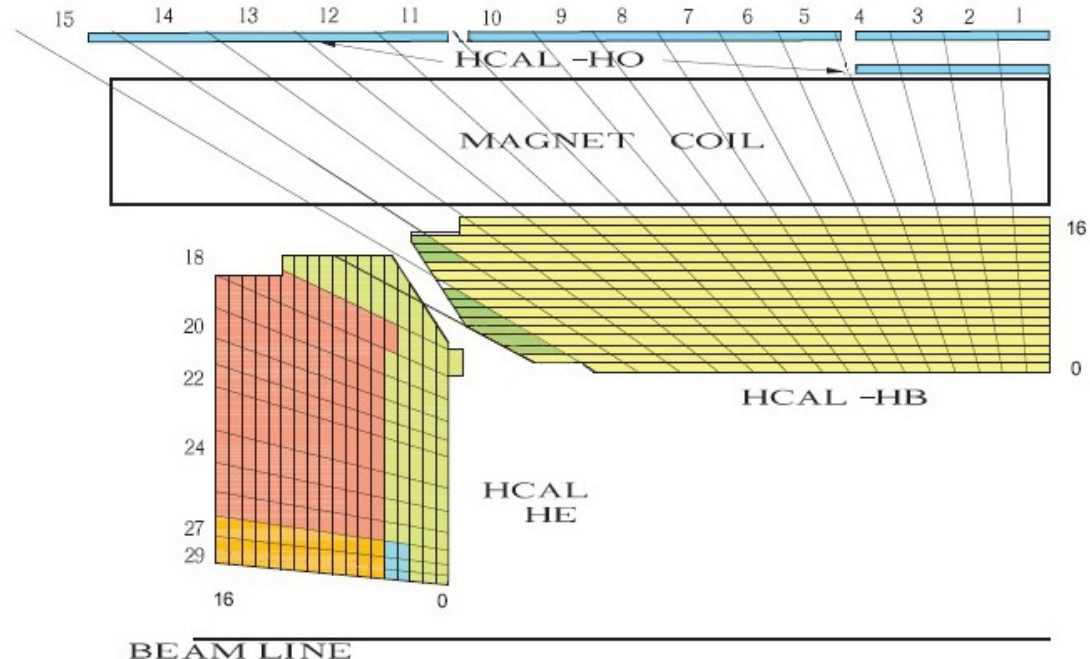


Figure 3.8: Diagram of HCAL geometry, reproduced from Ref. [3].

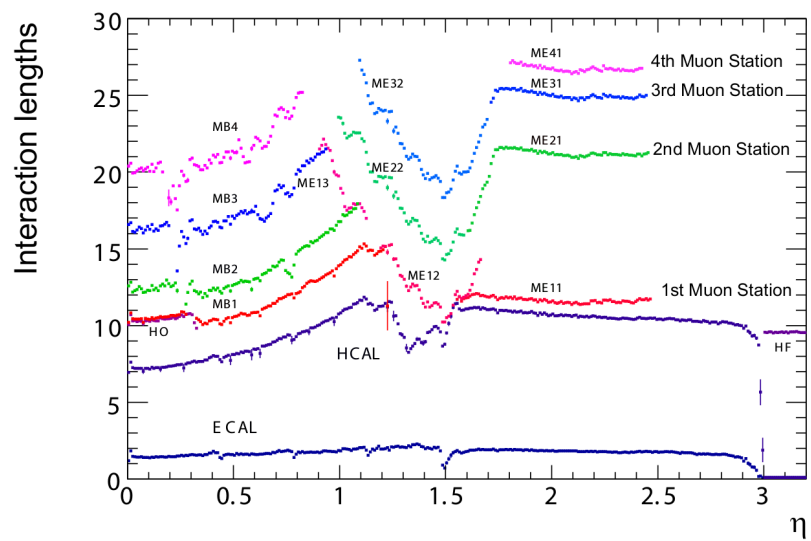


Figure 3.9: Total material budget in units of nuclear interaction lengths, as a function of pseudorapidity, reproduced from Ref. [3].

3.2.5 Muon Spectrometer

Many of the most interesting physics processes at the LHC involve high energy muons, so muon identification, triggering, and momentum measurement are important design goals. Muons leave very little energy in the calorimeters, so ECAL and HCAL cannot be used for triggering and identification as they are for electrons, photons and hadrons, or to improve momentum measurements of high- p_T muons whose tracks are too straight to allow good measurements of their curvature. Instead, these functions are provided for muons by three gas-based systems surrounding the rest of the detector. In all three, ionizing gas chambers provide hits which form a track. The magnetic field for this is provided by the return yoke, a set of steel plates interleaved with the muon chambers which confine the solenoid’s magnetic field. The yoke plates weigh a total of 10,000 t and are fully saturated by the solenoid.

Unlike the inner tracker, the muon systems can be read out fast enough to provide triggering. Because muons above 3 GeV generally traverse the muon system while most other measurable particles are stopped in the calorimeters, magnets, or return yoke, the muon system provides high efficiency, low-background muon identification. The muon system’s momentum measurements are not competitive with the inner tracker’s at low p_T , but a combined fit of the inner track and the muon system (“standalone”) track improves muon p_T resolution above roughly 200 GeV. The geometry of all three muon systems and the return yoke can be seen in Fig. 3.10.

3.2.5.1 Drift Tubes

In the barrel ($|\eta| < 1.2$), drift tube (DT) chambers are arranged in four “stations” separated by layers of the yoke. Stations are made of two or three superlayers (SLs) of four layers of rectangular drift cells. Adjacent layers are staggered latterally by half a cell width to avoid gaps. Each station has two SLs with wires running parallel

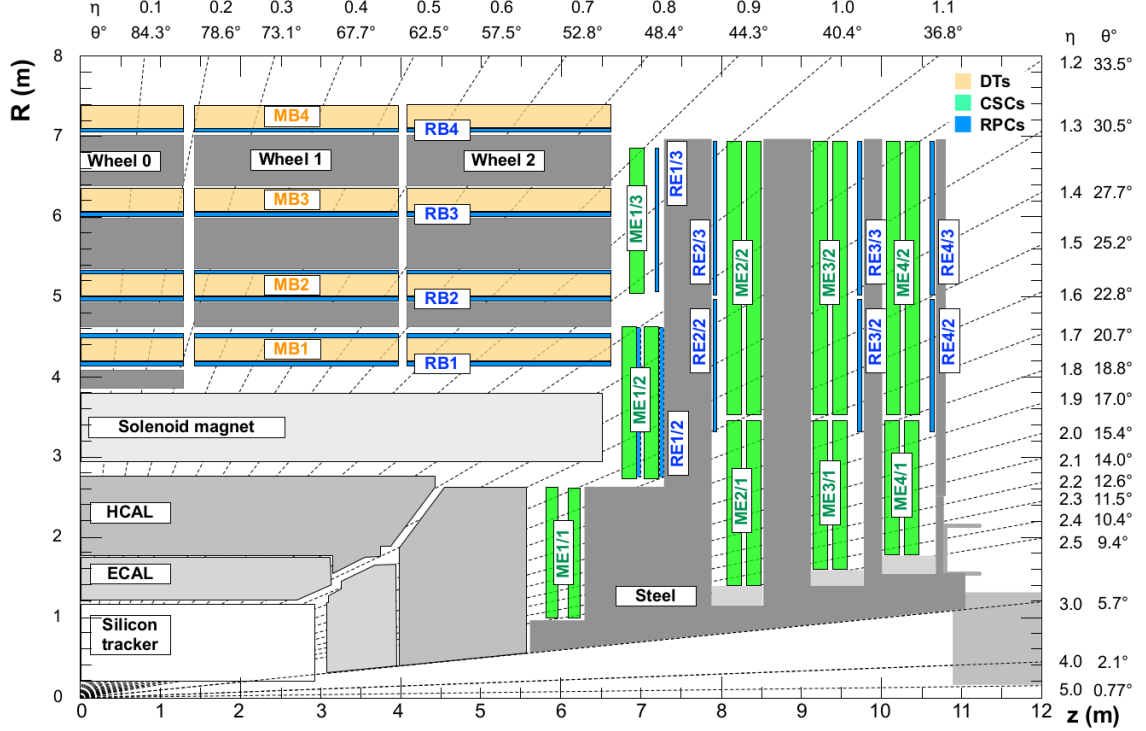


Figure 3.10: Diagram of muon system and return yoke geometry, reproduced from Ref. [17]. The magnet, calorimeters, and inner tracker are also visible.

to the beam to measure muon tracks in the $r\text{-}\phi$ plane, separated by an aluminum honeycomb lattice to provide mechanical rigidity and act as a spacer. The inner three stations contain an extra SL on the outer side of the spacer with wires perpendicular to the beam line, to measure muon position along the z -axis.

Each drift cell contains a roughly 2.4 m-long wire in gas (85% Ar, 15% CO₂). The electric field in the cell is provided by aluminum tape glued to the top and bottom of the cell and held at +1.8 kV relative to the grounded aluminum plates above and below. Aluminum tape cathodes on the side of the cell are held at -1.2 kV, while the wires act as +3.6 kV anodes. The width of each cell perpendicular to muon motion, 42 mm, was chosen for a maximum drift time of 380 ns, sufficient to obviate the need for double-hit readout logic in this low-occupancy region of the detector. The height of 13 mm set by mechanical and space constraints. Track timing resolution in each

SL is a few nanoseconds when all cells are allowed to read out all deposited charge. The $r\text{-}\phi$ position resolution available for online use in the trigger is about 1.5 mm in each SL; offline, for a single wire it is roughly 250 μm , leading to an overall resolution of 100 μm at each station.

3.2.5.2 Cathode Strip Chambers

Muons with $1.2 < |\eta| < 2.4$ are detected by the cathode strip chambers (CSCs).² The CSC system's trapezoidal chambers are arranged on discs interleaved with the endcap yoke in four layers. Chambers close to the beamline each cover 20° sections in ϕ , outer chambers cover 10° sections, with overlap to avoid gaps.

A CSC chamber is made of seven panels sandwiched together to make six gaps filled with a gas mixture (40% Ar, 50% CO₂, 10% CF₄). Six of the plates have cathode strips milled into one side, varying in pitch from 8.4 mm at the narrow end of the trapezoid to 16 mm at the wide end, with 0.5 mm gaps between strips. Three panels are wrapped with anode wires, alternating with the other panels so that every gas gap has a plane of wires. Wires are spaced 3.2 mm apart and run azimuthally around the detector, except for the innerpost chamber closest to the interaction point, which are inside the magnet and must have their wires tilted 29° so that charge collected by the wires moves parallel to them despite the Lorentz forces from the solenoid.

A typical muon will deposit charge in 3–4 cathode strips and a similar number of anode wires per gas gap, allowing hit position to be interpolated using all these signals as well as timing information. The single-plane spatial resolution can be as good as 80 μm but depends strongly on where in the width of the strip the muon hits. The strips in alternating planes are therefore offset by half their width. Measurements from all six gas gaps in a chamber are combined into a segment with position reso-

²Where the CSCs and DTs overlap ($0.9 < |\eta| < 1.2$), tracks are formed from hits in both.

lution in the $30\text{--}80\,\mu\text{m}$ range, which depends on the chamber but not where in the chamber the muon hit.

Anodes and cathodes are held 3.6 kV from each other, leading to a drift time of roughly 300 ns. Single anode planes have an RMS timing resolution of around 11 ns, insufficient for assigning a hit unambiguously to an individual bunch crossing, as required for triggering. However, information from all six anode planes in a chamber can be combined to yield a segment timing resolution around 5 ns. Segments are therefore the unit of information sent to the trigger. Segment position resolution at trigger level is 1–2 mm.

3.2.5.3 Resistive Plate Chambers

To provide a redundant set of muon momentum measurements, as well as precise timing of muon hits, CMS has six layers of resistive plate chambers (RPCs) in the barrel and four in the endcap up to $|\eta| < 1.6$. RPC chambers consist of two thin layers of inert gas (95.2% $\text{C}_2\text{H}_2\text{F}_4$, 4.5% C_4H_{10} , 0.3% SF_6) each between a pair of Bakelite electrodes held at 9.3 kV. The two “gas gaps” are placed on either side of a plane of copper strips. When a passing muon ionizes the gas, the high voltage causes a fast electron avalanche read out by the strips. The narrow gap allows the RPCs to have single-hit timing resolution around 1 ns, but the spatial resolution is limited to about 1 cm by the size of the readout strips. The DTs and CSCs both have better momentum resolution than the RPCs, but RPCs are a simple, robust auxiliary system and the timing resolution can be used in conjunction with the other systems to improve overall muon measurements.

3.2.6 Data Acquisition and Trigger

With a bunch crossing rate of 40 MHz giving a collision rate that can exceed 1.6 GHz and raw event sizes of 1–2 MB, the raw data generation rate of CMS could potentially be several PB/s, substantially more than can be read out, stored or analyzed with current technology. However, most events consist only of low-energy, well-understood QCD interactions, so the data rate can be drastically reduced by reading out and storing only events likely to have interesting physics content. CMS reduces the event rate with a two-level trigger system.

The level-1 (L1) trigger uses custom hardware operating on trigger primitives (TPs), low-granularity detector information, to reduce the event rate to 100 kHz or less. Inner tracker readout is too slow for use in the trigger, so only the calorimeters and muon systems generate TPs. Events accepted at level-1 are read out, digitized, and sent to the high level trigger (HLT), where they are partially reconstructed in software and filtered further, reducing the final rate of stored events to roughly 1 kHz.

3.2.6.1 Level-1 Trigger

LHC beams collide at too high a rate for trigger decisions to be made in software, so the L1 trigger is instead implemented in custom hardware, with processing done using field-programmable gate arrays (FPGAs) as much as possible for flexibility, and application-specific integrated circuits (ASICs) where required. Hardware limitations of other CMS subsystems—in particular, the inner tracker’s readout speed and buffer capacity—impose strict constraints on the system. The rate of events passing at level-1 cannot exceed 100 kHz and the system’s overall latency cannot exceed roughly $4.2\ \mu\text{s}$. These goals are achieved while maintaining high efficiency for interesting physics events by using only low-granularity detector information, to reduce the bandwidth needed within the trigger system. Information flows through

subsystems, with the amount of data reduced at each step. Calorimeter and muon information are processed in parallel and combined only in the final step. Optical links between systems provide high-bandwidth data transfer and allow flexibility in the overall trigger architecture. The calorimeter trigger was upgraded with respect to the Run I configuration in 2015, and the whole trigger system was overhauled in 2016 [18]. Both configurations will be described here.

Calorimeter information is compressed into trigger primitives (TPs) for use in the trigger by trigger primitive generators (TPGs). Each TP represents a “tower” consisting of a 5×5 cluster of barrel or endcap ECAL crystals and the portion of HCAL behind them, or a section of the HF. The TP contains an 8-bit transverse energy sum and a quality bit for each calorimeter, and six bits of error checking and bookkeeping information. In 2015, TPs were sent to the Regional Calorimeter Trigger (RCT), which processed 18 portions of the detector (segmeted in ϕ with $+\eta$ and $-\eta$ treated separately) in parallel in separate crates of electronics, using several ASICs and one FPGA in each crate for processing. Each RCT crate summed the TPs with $|\eta| < 3.0$ into 4×4 tower regions, and found isolated and non-isolated 2×1 tower e/ γ and τ candidates. These objects were sent to Stage 1 Layer 2, which selected the best e/ γ and τ candidates from the entire detector, clustered regions into 3×3 region jet candidates, and computed global quantities like missing transverse energy and the scalar sum of transverse momentum for all particles in the event. Pileup subtraction was performed with a lookup table (LUT) based on the number of regions in the detector with no energy.

In 2016, the whole calorimeter trigger was replaced with a new two-tiered system. Stage 2 Layer 1 (“CaloL1”) consists of 18 FPGA-based Calorimeter Trigger Processor 7 (CTP7) cards, which calibrate and reformat the TPs before forwarding them to Stage 2 Layer 2 (“CaloL2”), an FPGA-based time-multiplexed system which finds

e/γ , τ , and jet candidates and computes global quantities for whole events in parallel using tower-level information.

In 2015, the DTs and CSCs fed track segments into track finders (DTTF and CSCTF) which used pattern recognition algorithms to reconstruct tracks and measure their p_T , sharing information between the track finders to avoid inefficiency in the overlap region. The RPCs made their own tracks. Since the 2016 upgrade, track finding has been done by geometrical region of the detector rather than detector subsystem alone, with separate track finders for the barrel (BMTF, $|\eta| < 0.85$), endcap (EMTF, $1.25 < |\eta| < 2.4$) and overlap (OMTF, $0.85 < |\eta| < 1.25$) regions. The track finders feed into the Global Muon Trigger (GMT, upgraded to μ GMT in 2016), which merges and sorts tracks, analyzes their quality and selects the best ones.

The calorimeter and muon trigger systems, which have up to this point worked entirely in parallel, both send their selected candidates and global quantities to the Global Trigger (GT, upgraded to μ GT). The Global Trigger contains the trigger menu, the configurable set of algorithms used to determine whether an event is accepted or not. These algorithms can use combinations of the objects from the calorimeter and muon trigger systems, including imposing topological requirements, e.g. requiring a large $\Delta\eta$ between muons in a pair. The final decision is a logical OR of all triggers in the menu, but each trigger may be prescaled, i.e. only included in the final decision a fraction of the time in order to reduce its rate. When an event is accepted, a level 1 accept (L1A) signal is sent to all CMS subsystems instructing them to read out information collected in the accepted event, which is stored in buffers until it can be read out or safely discarded. A diagram of the whole 2016 L1 trigger system and its information flow is shown in Fig. 3.11.

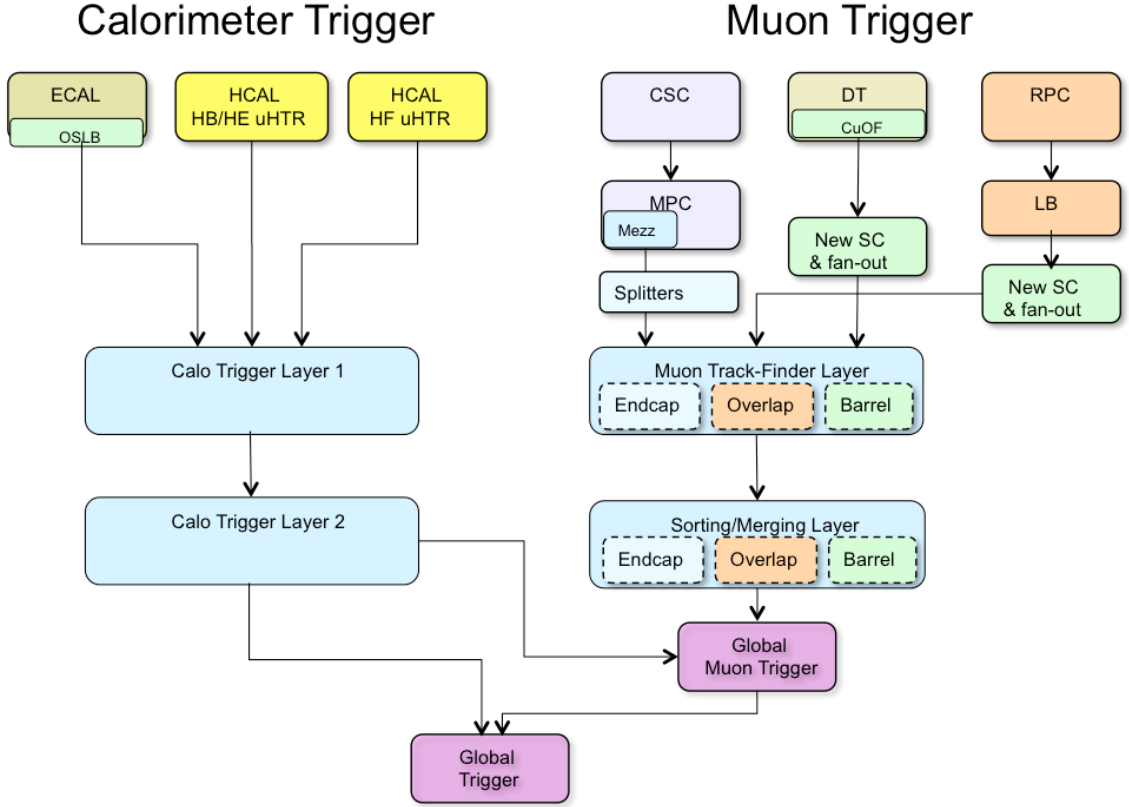


Figure 3.11: Data flow diagram for the CMS L1 trigger after the 2016 overhaul, reproduced from Ref. [18].

3.2.6.2 High-Level Trigger

After an accepted event is read out and digitized, it must undergo another level of screening before being stored. The High Level Trigger (HLT) uses full detector information reconstructed with versions of the normal CMS reconstruction algorithms specially optimized for speed, running on a large farm of commercial computers. Much of HLT's power comes from having tracker information, allowing more precise momentum measurements, isolation calculations and identification algorithms than are available at L1. For example, the pixels can be used to reconstruct vertices and tag b-quark jets, and requirements can be placed on the invariant mass of a lepton pair. However, track reconstructions is slow, so it is typically only done as one of the

last steps in the filtering process, allowing the event to be rejected based on more easily reconstructed objects like tracks in the muon system. Other optimizations include only reconstructing tracks near objects passed in by the L1 Global Trigger. The final result is that the rate of events saved for later analysis is around 1 kHz.

3.2.7 Luminosity Determination

A precise measurement of the luminosity delivered by the LHC is critical to precisely measuring any cross section. The instantaneous luminosity for n_b colliding bunch pairs with intensity N_b and orbit frequency f_{rev} is given by

$$\mathcal{L} = \frac{n_b N_b^2 f_{rev}}{A_{\text{eff}}} \quad (3.14)$$

where A_{eff} is the effective area of the beam-beam overlap. If beam i has a gaussian density profile in the u direction of width $\sigma_{i,u}$, and the beam densities are uncorrelated in each direction, then

$$A_{\text{eff}} = 2\pi \sqrt{\sigma_{1,x}^2 + \sigma_{2,x}^2} \sqrt{\sigma_{1,y}^2 + \sigma_{2,y}^2}. \quad (3.15)$$

The beam widths $\sigma_{i,u}$, the only unknowns in Eq. 3.14, are purely geometrical and can be found with the Van de Meer (VdM) scan method [19, 20]. In a VdM scan, for which LHC has a special run mode, one beam is held fixed while the position of the other is scanned in the x - y plane, and detector activity is measured as a function of beam displacement. Because the width of the interaction rate distribution is independent of its overall normalization, the detector activity metric may be any quantity linearly proportional to the interaction rate.

Over the course of an LHC run, n_b , N_b , and A_{eff} are all subject to change, and in fact the VdM scans are performed with a special LHC configuration, so in practice the procedure outlined above provides a calibration and overall scale for luminosity

measurements during physics collisions. For a given detector metric labeled Q with rate R^Q that peaked at R_0^Q with no beam displacement, the VdM scan yields a visible cross section, the constant of proportionality between the rate and the instantaneous luminosity,

$$\sigma_{\text{vis}}^Q \equiv \frac{R^Q}{\mathcal{L}} = A_{\text{eff}} R_0^Q. \quad (3.16)$$

CMS has several such metrics; the primary one used for measuring integrated luminosity is the number of pixel hit clusters [21, 22]. The instantaneous luminosity is given by

$$\mathcal{L} = \frac{\langle N_c \rangle f_{\text{rev}}}{\sigma_{\text{vis}}^{\text{PCC}}} = \frac{\langle N_c \rangle}{A_{\text{eff}} \langle N_c \rangle_0} \quad (3.17)$$

where $\langle N_c \rangle$ is the average number of pixel hit clusters at each bunch crossing and $\langle N_c \rangle_0$ is its peak value during the VdM scan.

A number of complications must be accounted for or included in systematic uncertainty estimates. Beam-beam interaction effects, correlations between the proton density distributions in the x and y directions, drifts in the beam orbit, and normalization uncertainties on the bunch intensity and absolute distance scale from the beam spot must all be handled with care. The result is a total integrated luminosity uncertainty of 2.3% in 2015 and 2.5% in 2016.

Chapter 4

Simulation

4.1 Monte Carlo Event Generation

It's like gambling

4.1.1 Matrix Element Generation

The real physics

4.1.2 Parton Shower, Hadronization, and Underlying Event

The way-too-real physics

4.1.3 Pileup Simulation

Lots of it

4.2 Detector Simulation

All kinds of fun

Chapter 5

Object Reconstruction and Selection

5.1 Track Reconstruction and Vertex Identification

So many fits

5.2 Particle Flow Reconstruction

The overview

5.2.1 PF Candidates

5.2.1.1 Muons

yep

5.2.1.2 Electrons and Charged Hadrons

uh huh

5.2.1.3 Photons and Neutral Hadrons

yeah

5.2.2 Jets

sure

5.2.3 Missing Transverse Energy

ok

5.3 Object Identification and Selection

What to use in the actual analysis

5.3.1 Electrons

nice

5.3.2 Muons

even nicer

5.3.3 Jets

not as nice

5.3.4 Final State Photon Radiation

Bit of a mess

5.3.5 Misidentified Objects

Fake rates

5.4 ZZ Candidate and Event Selection

Explain the different classes of events (full spectrum, Higgs, on shell...)

5.4.1 Z Candidate Selection

Mass cuts and lepton pairing

5.4.2 ZZ Candidate Selection

Disambiguation for 4 leptons

5.4.3 Background Estimation

5.4.4 VBS Signal Selection

Dijets and so on

Chapter 6

Analysis Strategy

6.1 Background Estimation

Reducible backgrounds for four-lepton events typically have two prompt leptons and two other objects—typically jet fragments, sometimes photons—which are misidentified as prompt leptons. The largest source of background contamination is from events in which a Z boson is produced in association with a photon and a jet, a leptonically-decaying W boson and a jet, or two jets. There is also a contribution from tt events in which both top quarks decay to a lepton, a neutrino, and a b quark jet. For simplicity, the two sets of processes are not treated separately in what follows, and are collectively labeled “Z + X” events.

The contributions of the reducible backgrounds to the selected four-lepton signal samples are evaluated using the tight-to-loose “fake rates” method, described more fully in Ref. [23]. In this procedure, the likelihood of a nonprompt (“fake”) object to be misidentified as a prompt lepton is estimated and applied to control regions enriched with Z + X events to estimate their contribution to the signal region. The lepton misidentification rate $f_\ell(p_T^\ell, \eta^\ell)$ is measured from a sample of Z + ℓ_{fake} events,

where the Z candidate is selected as in the signal region but with $|m_{\ell\ell} - m_Z| < 10 \text{ GeV}$, and the ℓ_{fake} object is a lepton candidate that passes relaxed ID requirements as defined in Section 5.3.5, with no isolation or tight ID requirements applied. Events with three prompt leptons can contaminate this control region, because the non-Z lepton is assumed fake. To avoid the resulting bias in the misidentification rate, the contribution of $WZ \rightarrow 3\ell\nu$ to the $Z + \ell_{\text{fake}}$ sample is estimated from a simulated sample and subtracted.

The misidentification rate is defined as the fraction of ℓ_{fake} candidates which pass full lepton identification and isolation criteria, in bins of p_T and η . One should note that this is not a probability in the usual sense, and there is not a simple physical interpretation of these misidentification rates. Figure 6.1 shows the misidentification rates for electrons and muons separately as a function of p_T and η .

To estimate the total reducible background yield, the misidentification rates are applied to two $Z + X$ enriched control samples, each containing a Z boson candidate passing all signal region requirements plus two more lepton candidates which pass the relaxed identification criteria and would make a second passing Z boson candidate except that one or both fail the full identification or isolation criteria. The sample with one failing lepton, called the “3P1F” sample for “3 prompt 1 fake,” covers the contribution from WZ events, while the sample with both leptons in the second Z boson failing (“2P2F”) covers Z+jets and $t\bar{t}$ events. Both have the contribution from ZZ events in which one or two prompt leptons fail identification or isolation criteria removed based on simulated samples. The fake object transfer factor

$$F_\ell(p_T^\ell, \eta^\ell) = \frac{f_\ell(p_T^\ell, \eta^\ell)}{1 - f_\ell(p_T^\ell, \eta^\ell)} \quad (6.1)$$

is the ratio of nonprompt objects passing the relaxed and full selection criteria, and thus serves as an extrapolation factor between control sample yields and signal sample

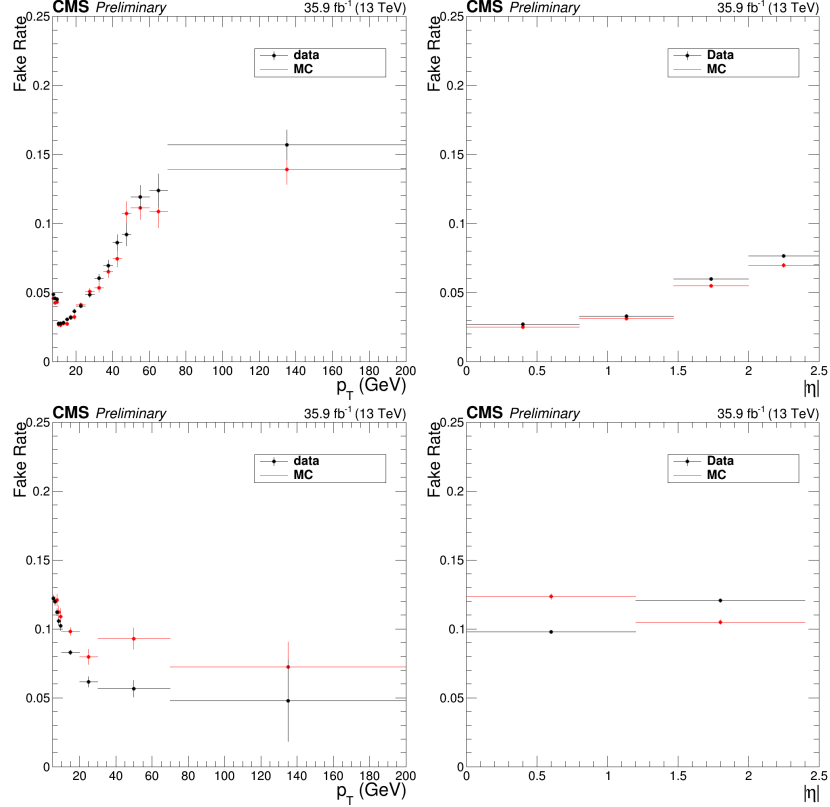


Figure 6.1: Fake rate for electrons (top) and muons (bottom) as a function of p_T (left) and η (right).

yields.

The total reducible background yield is thus

$$N_{\text{bkg}} = \sum_{\ell \in 3\text{P}1\text{F}} F_\ell(p_T^\ell, \eta^\ell) - \sum_{\ell_1, \ell_2 \in 2\text{P}2\text{F}} F_{\ell_1}(p_T^{\ell_1}, \eta^{\ell_1}) F_{\ell_2}(p_T^{\ell_2}, \eta^{\ell_2}), \quad (6.2)$$

where subtraction of signal contamination is implicit. The minus sign in Eq. 6.2 prevents double-counting of Z+2jets events in which one jet fragment is misidentified.

There are also irreducible background contributions from $t\bar{t}Z$ and WWZ events, which can have four prompt leptons. Expected yields for these processes are taken from simulation.

6.2 Systematic Uncertainties

Systematic uncertainties for trigger efficiency are taken to be the difference between trigger efficiencies in data and in simulated events, found to be around 2% of the final event yield. Because leptons in $Z \rightarrow 4\ell$ events generally have lower p_T , the uncertainty increases to 4% for $Z \rightarrow 4e$ events. In both data and simulated events, trigger efficiencies are found with a tag-and-probe technique [24], performed on four-lepton events.

The lepton identification and isolation efficiencies in simulation are corrected with scaling factors derived with the tag-and-probe method, performed on a sample of $Z \rightarrow \ell^+\ell^-$ events. To find the uncertainties associated with these corrections, the total yield is recomputed with the scaling factors varied up and down by the tag-and-probe uncertainties, treating all bins as correlated. The uncertainties in the $ZZ \rightarrow 4\ell$ yield associated with the tag-and-probe results are found to be 6% in the 4e final state, 3% in the 2e2 μ final state, and 2% in the 4 μ final state. Leptons in $Z \rightarrow 4\ell$ events tend to have lower p_T , and the tag-and-probe samples for low- p_T leptons are smaller and more contaminated with nonprompt objects, so the uncertainties are larger; they are found to be 10%, 6%, and 7% for the 4e, 2e μ , and 4 μ final states, respectively.

The uncertainty on the LHC integrated luminosity of the data sample is 2.5%.

The uncertainty on lepton fake rates is taken to be 40%, which includes both statistical uncertainty and systematic uncertainties associated with the loosened lepton selections used and the differences in the underlying physics processes between events in the 3ℓ and 4ℓ control samples. Statistical uncertainties arising from the limited size of the $Z + X$ control samples is also included as a systematic uncertainty on the background yield. The total uncertainty on the background yield varies by channel

but is below 1% of the expected total yield.

Uncertainties due to the effect of QCD scale on the $ZZ \rightarrow 4\ell$ acceptance are evaluated with `POWHEG` and `MCFM`, by varying the QCD scales up and down by a factor of two with respect to the default $\mu_R = \mu_F = m_{ZZ}$. Parametric uncertainties ($\text{PDF} + \alpha_s$) are evaluated according to the `PDF4LHC` prescription in the acceptance calculation [25], and with `NNPDF3.0` in the cross section calculations. An additional theoretical uncertainty arises from scaling the $q\bar{q} \rightarrow ZZ$ and $gg \rightarrow ZZ$ simulated samples to their NNLO and NLO predicted cross sections, respectively. The corresponding change in the acceptance, 1.1%, is added to the previous theoretical errors in quadrature.

Systematic uncertainties on expected signal yield are summarized in Table 6.1. To obtain uncertainties in computed quantities such as cross sections, the inputs are varied separately for each source and the calculation is fully redone. For differential cross section and other shape uncertainties, the variations across bins are taken to be fully correlated for each uncertainty source. Lepton and jet momentum scale and resolution uncertainties are taken to be trivial for the overall yield, but they are considered among the shape uncertainties.

6.3 Fiducial and Total Cross Section Calculation

Inclusive cross section measurements can be treated as simple binned counting experiments, where the bins are the three decay channels ($4e$, $2e2\mu$, and 4μ). If ν events are expected in a given bin, the probability of observing n events is given by the Poisson distribution,

$$f(n; \nu) = e^{-\nu} \frac{\nu^n}{n!}. \quad (6.3)$$

Table 6.1: The contributions of each source of signal systematic uncertainty in the total yields. The integrated luminosity uncertainty and the PDF and scale uncertainties are considered separately. All other uncertainties are added in quadrature into a single systematic uncertainty. Uncertainties that vary by decay channel are listed as a range.

Uncertainty	$Z \rightarrow 4\ell$	$ZZ \rightarrow 4\ell$
Lepton efficiency	6–10%	2–6%
Trigger efficiency	2–4%	2%
MC statistics	1–2%	0.5%
Background	0.6–1.3%	0.5–1%
Pileup	1–2%	1%
PDF	1%	1%
QCD Scales	1%	1%
Integrated luminosity	2.5%	2.5%

In a particle physics analysis like this one, ν takes the form

$$\nu = \nu_s(\vec{\theta}_s) + \nu_b(\vec{\theta}_b) = \mu(\vec{\theta}_s) \mathcal{L}_{int} \sigma_{SM} \epsilon + \nu_b(\vec{\theta}_b) \quad (6.4)$$

where ν_s and ν_b are respectively the expected signal and background yields, σ_{SM} is the standard model expectation for the cross section of the signal process and ϵ is our efficiency for detecting and identifying its events. The signal and background nuisance parameter vectors $\vec{\theta}_s$ and $\vec{\theta}_b$ represent hidden quantities that we do not measure directly but which affect our yields, i.e. systematic effects. The signal strength μ compares our expectation to what we actually measure:

$$\mu = \frac{\sigma_{meas}}{\sigma_{SM}}. \quad (6.5)$$

Of the variables in Eqs. 6.3 and 6.4, σ_{SM} is known from theoretical calculations, and ϵ is determined from simulation. The CMS detector is designed to measure n , ν_b , and \mathcal{L}_{int} , and inferring σ_{meas} is a matter of working backwards to the most likely value of the signal strength μ given the observed data. Then the measured cross

section is simply

$$\sigma_{meas} = \mu\sigma_{SM}. \quad (6.6)$$

One interesting feature of this method is that σ_{SM} is used in the calculation of μ (Eq. 6.4) and in the final cross section (Eq. 6.6) in such a way that it cancels out, and in fact anything proportional to the true cross section may be used. In practice, this means that the order at which σ_{SM} is calculated does not matter to the extent that higher order corrections to the kinematics of the events do not affect ϵ .

6.3.1 Signal Strength Extraction

The signal strength is found by the method of maximum likelihood [26, 27]. The likelihood function is the product of the probability distributions across all bins,

$$L\left(\vec{\theta}_s, \vec{\theta}_b\right) = \prod_{bins} f\left(n; \nu\left(\vec{\theta}_s, \vec{\theta}_b\right)\right). \quad (6.7)$$

The most likely value of ν is the one that maximizes L . In practice, $\log L$ is typically maximized instead because it is easier to work with,

$$\frac{\partial^2 \log L}{\partial \vec{\theta}_s \partial \vec{\theta}_b} = 0. \quad (6.8)$$

This maximization is performed simultaneously for all bins, yielding a single signal strength across all channels. Systematic uncertainties enter as log-normal constraints imposed on the fit, encoded in $\vec{\theta}_s$ and $\vec{\theta}_b$. The fit is performed numerically.

6.3.2 Total ZZ Cross Section and Z → 4ℓ Branching Fraction

Once the fiducial cross section has been found, it can be used to find the total cross section, subject only to the constraint that both Z bosons be in the 60–120 GeV mass range. The fiducial cross section is related to the total cross section by an acceptance

factor \mathcal{A} which accounts for $ZZ \rightarrow 4\ell$ events outside the fiducial definition, and two factors of the Z branching fraction $\mathcal{B}(Z \rightarrow 2\ell)$ to account for all other final states:

$$\sigma_{fid} = \mathcal{A}\sigma_{tot} (\mathcal{B}(Z \rightarrow 2\ell))^2. \quad (6.9)$$

The acceptance factor is independent of any experimental effects and can be calculated from Monte Carlo events at generator level. The Z branching fraction is well known [26].

The total Z cross section is better measured in the 2ℓ channel, because the larger branching fraction yields samples several orders of magnitude larger than the $Z \rightarrow 4\ell$ sample used here. It is therefore more interesting to use $\sigma_{fid}(Z \rightarrow 4\ell)$ for a measurement of the four-lepton branching fraction $\mathcal{B}(Z \rightarrow 4\ell)$. After applying the acceptance correction to obtain $\sigma_{tot}(Z \rightarrow 4\ell) = \sigma_{fid}(Z \rightarrow 4\ell) / \mathcal{A}$, the four-lepton branching fraction is given by

$$\mathcal{B}(Z \rightarrow 4\ell) = \frac{\sigma_{tot}(Z \rightarrow 4\ell)}{\mathcal{C}_{80-100}^{60-120} \sigma(Z \rightarrow 2\ell)} \mathcal{B}(Z \rightarrow 2\ell), \quad (6.10)$$

where $\sigma(Z \rightarrow 2\ell)$ is the dileptonic Z cross section in the 60–120 GeV mass range and $\mathcal{C}_{80-100}^{60-120}$ corrects for the fact that $\sigma(Z \rightarrow 4\ell)$ is found in a mass range of 80–100 GeV.

6.4 Differential Cross Sections

Measurement of a differential fiducial cross section is also a problem of finding the most likely true distribution given observed yields in multiple bins, estimated background yields, and detector effects understood through simulation. Unlike the inclusive cross section, however, finite detector resolution leads to “smearing” effects that cause events to migrate across bins, in addition to the same inefficiencies. The mean detector-level distribution $\vec{\delta}$ is related to the true distribution $\vec{\theta}$ by a response matrix \mathbf{R} :

$$\vec{\delta} = \mathbf{R}\vec{\theta}. \quad (6.11)$$

The observed distribution in data \vec{d} is sampled from the Poisson distribution with mean $\vec{\delta}$ independently in each bin. CMS simulation software is sufficiently sophisticated to give a good estimate of R . Note that the case of bins with no migration, as in the inclusive cross section measurement, is the special case where \mathbf{R} is diagonal.

If \mathbf{R} is square and invertible, the maximum likelihood estimate (MLE) of the true distribution, $\hat{\vec{\theta}}$, is given by

$$\hat{\vec{\theta}} = \mathbf{R}^{-1} \vec{d}. \quad (6.12)$$

Even when \mathbf{R} is invertible, however, it is frequently ill-conditioned, giving $\hat{\vec{\theta}}$ unphysical features like large bin-by-bin fluctuations or even negative bins as a consequence of the stochastic nature of \vec{d} . It is therefore necessary to use a more sophisticated procedure to ensure the differential cross section distributions obey physics-inspired constraints.

6.4.1 Unfolding

The technique used here is an iterative frequentist method developed in high energy physics by D'Agostini [28] and independently in other fields [29–32], as implemented in ROOUNFOLD [33]. At iteration k , bin j of the predicted true distribution is set based on its expected contribution to all other bins, weighted by the observed data yield in each:

$$\begin{aligned} \theta_j^{(k+1)} &= \sum_i \mathbf{R}_{ij} \theta_j^{(k)} \frac{d_i}{\delta_i} \\ &= \sum_i \mathbf{R}_{ij} \theta_j^{(k)} \frac{d_i}{\sum_m \mathbf{R}_{im} \theta_m^{(k)}}. \end{aligned} \quad (6.13)$$

After several iterations, $\vec{\theta}^{(k)}$ depends only weakly on the ansatz $\vec{\theta}^{(0)}$.

The sequence will converge to the MLE for any non-pathological choice of $\vec{\theta}^{(0)}$ [34], but again the MLE often displays unphysical behavior. If $\vec{\theta}^{(0)}$ is strictly positive, $\vec{\theta}^{(k)}$ will be strictly positive for all k , and in this case $\hat{\vec{\theta}}$ (as defined in Eq. 6.12) will be

the asymptotic unfolded distribution as long as it is also strictly positive. Choosing a smooth function for $\vec{\theta}^{(0)}$ will generally lead to smooth $\vec{\theta}^{(k)}$ for small k ; typical choices include a flat initial distribution and the truth-level distribution used to construct \mathbf{R} (used in this analysis). What constitutes “small” k depends on the condition of \mathbf{R} , but for most physics distributions of interest, including all those used in this analysis, nonphysical fluctuations do not arise until after $\vec{\theta}^{(k)}$ is close to convergence. Full regularization is therefore imposed by ceasing iteration early. For all distributions shown here, stopping after four iterations was found to give acceptable bias-variance tradeoff.

6.4.2 Uncertainties

The largest uncertainties in the unfolded distributions arise from the unfolding procedure itself, which can inflate statistical uncertainties present in the detector-level distributions. The correlation matrix which gives the full uncertainty—considered the statistical uncertainty of the unfolded distribution—does not have a closed form due to the nonlinearity of the method. The covariance matrix is therefore estimated by propagating the statistical error of the inputs at each iteration of the method, as laid out in Ref. [28] and improved in Ref. [33]. This procedure does not account for the bias introduced by regularization, but this is expected to be negligible relative to other systematic uncertainties for the well-modeled processes studied here.

Most systematic uncertainties are propagated through unfolding by recomputing the response matrix with the training sample shifted or reweighted to reflect a 1σ shift in the quantity in question. The uncertainty related to that quantity is taken to be the resulting shape difference in the final unfolded distribution. Systematic uncertainties are negligible compared to statistical uncertainties in most bins.

6.5 VBS Signal Extraction

The VBS signal search considers events passing the selections described in Section 5.4.4. The electroweak yield is insufficient to have sensitivity at 35.9 fb^{-1} , even with further cut optimization, so a gradient-boosted decision tree (GBDT), implemented with the SCIKIT-LEARN package [35], is used to extract the signal. Hyperparameters of the GBDT are optimized with a grid search. Each Monte Carlo sample is split into a “training” subsample, used to train the GBDT, and a “test” subsample used to evaluate its performance and make templates for use in the statistical analysis. The GBDT performance is nearly the same for the test and training samples, a sign that the algorithm is not overtrained.

A number of observables have been proposed to discriminate VBS events from background [36], of which m_{jj} and $\Delta\eta_{jj}$ are the most powerful. Other commonly-used variables include $m_{4\ell}$, $\eta^{j_1} \times \eta^{j_2}$, $\Delta\phi_{Z_1 Z_2}$, and the so-called Zeppenfeld variables, defined as

$$\eta_P^* = \eta_P - \frac{\eta_{j_1} - \eta_{j_2}}{2}, \quad (6.14)$$

where P may stand for Z_1 , Z_2 , or j_3 , the highest- p_T untagged jet in the event. In addition to these “traditional” quantities, several other groups of observables have been examined, including production angles, decay angles, measures of total hadronic activity in the event, properties of individual leptons and jets and of the $ZZjj$ system, and a discriminator designed to distinguish jets originating from quarks and gluons. The hadronic activity and quark-gluon tagging variables had some discriminating power, but they differ significantly depending on the Monte Carlo generator used and were therefore considered too poorly-modeled to use. New GBDTs were trained, each with the traditional observables and one remaining group of proposed observables, and the groups that improved the GBDT discrimination power significantly were

retained. This procedure yielded 17 observables, including the hard process relative transverse momentum, defined as the ratio of the p_T of the ZZjj system to the scalar sum of the p_T of each object,

$$p_T^{rel.\ hard} = \frac{p_T^{ZZjj}}{\sum_{Z_1, Z_2, j_1, j_2} p_T}, \quad (6.15)$$

and the dijet relative transverse momentum,

$$p_T^{rel.\ jj} = \frac{p_T^{jj}}{\sum_{j_1, j_2} p_T}. \quad (6.16)$$

The list of observables was further optimized by retraining the GBDT once with each variable dropped and eliminating the one with the least discriminating power. This pruning was repeated until seven observables remained, namely m_{jj} , $\Delta\eta_{jj}$, $m_{4\ell}$, $\eta_{Z_1}^*$, $\eta_{Z_2}^*$, $p_T^{rel.\ hard}$, and $p_T^{rel.\ jj}$. The resulting GBDT performs only marginally worse (0.2 σ less expected significance on the VBS signal) than a version with all observables included, and is faster and easier to train, simpler, and less susceptible to biases and systematic uncertainties from mismodeling.

The signal and background yields are extracted from the GBDT output spectrum are extracted with a binned maximum likelihood fit to templates from the test Monte Carlo samples. To obtain templates with better fit convergence properties, the GBDT output is mapped to the range [0, 1] with the logistic transformation

$$x \rightarrow \frac{1}{1 - e^{-x}}. \quad (6.17)$$

This provides better separation between signal and background and allows uniform binning in the templates.

6.6 Anomalous Gauge Coupling Searches

Chapter 7

Results

7.1 Four-Lepton Yield and Distributions

7.1.1 Full Spectrum

Everything

7.1.2 $Z \rightarrow 4\ell$ Resonance

Found it

7.1.3 Higgs Resonance

Found it too

7.1.4 ZZ Production

Including ZZ+jets

7.2 ZZ Fiducial and Total Cross Section

The big thing

7.2.1 $Z \rightarrow 4\ell$ Branching Fraction

A nice little measurement

7.3 Differential Cross Sections

With awesome plots

7.4 Vector Boson Scattering

Electroweak signal's electrostrength

7.5 Anomalous Coupling Limits

Winning at not finding things

Chapter 8

Conclusions

8.1 Summary

8.2 Outlook

Bibliography

- [1] L. Evans and P. Bryant, “LHC machine,” *JINST*, vol. 3, S08001, 2008. DOI: 10.1088/1748-0221/3/08/S08001.
- [2] O. Brüning, H. Burkhardt, and S. Myers, “The large hadron collider,” *Prog. Part. Nucl. Phys.*, vol. 67, no. 3, pp. 705–734, 2012, ISSN: 0146-6410. DOI: <https://doi.org/10.1016/j.ppnp.2012.03.001>. [Online]. Available: <http://www.sciencedirect.com/science/article/pii/S0146641012000695>.
- [3] CMS Collaboration, “The CMS experiment at the CERN LHC,” *JINST*, vol. 3, S08004, 2008. DOI: 10.1088/1748-0221/3/08/S08004.
- [4] C. Lefèvre, “The CERN accelerator complex. complexe des accélérateurs du CERN,” Dec. 2008, [Online]. Available: <https://cds.cern.ch/record/1260465>.
- [5] ATLAS Collaboration, “The ATLAS experiment at the CERN large hadron collider,” *JINST*, vol. 3, S08003, 2008. DOI: 10.1088/1748-0221/3/08/S08003.
- [6] LHCb Collaboration, “The LHCb detector at the LHC,” *JINST*, vol. 3, S08005, 2008. DOI: 10.1088/1748-0221/3/08/S08005.
- [7] ALICE Collaboration, “The ALICE experiment at the CERN LHC,” *JINST*, vol. 3, S08002, 2008. DOI: 10.1088/1748-0221/3/08/S08002.
- [8] TOTEM Collaboration, “The TOTEM experiment at the CERN large hadron collider,” *JINST*, vol. 3, S08007, 2008. DOI: 10.1088/1748-0221/3/08/S08007.
- [9] LHCf Collaboration, “The LHCf detector at the CERN large hadron collider,” *JINST*, vol. 3, S08006, 2008. DOI: 10.1088/1748-0221/3/08/S08006.
- [10] MoEDAL Collaboration, “The physics programme of the MoEDAL experiment at the LHC,” *Int. J. Mod. Phys.*, vol. A29, p. 1430050, 2014. DOI: 10.1142/S0217751X14300506. arXiv: 1405.7662 [hep-ph].

- [11] M. Bajko *et al.*, “Report of the task force on the incident of 19th September 2008 at the LHC,” CERN, Geneva, Tech. Rep. LHC-PROJECT-Report-1168. CERN-LHC-PROJECT-Report-1168, Mar. 2009. [Online]. Available: <http://cds.cern.ch/record/1168025>.
- [12] M. Lamont, “Status of the LHC,” *Journal of Physics: Conference Series*, vol. 455, no. 1, p. 012001, 2013. [Online]. Available: <http://stacks.iop.org/1742-6596/455/i=1/a=012001>.
- [13] Y. Papaphilippou, H. Bartosik, G. Rumolo, and D. Manglunki, “Operational beams for the LHC,” 2014. arXiv: 1412.7857 [physics.acc-ph].
- [14] F. Bordry and C. Pralavorio, “LHC smashes targets for 2016 run,” Nov. 2016. [Online]. Available: <http://cds.cern.ch/record/2235979>.
- [15] T. Sakuma and T. McCauley, “Detector and event visualization with SketchUp at the CMS experiment,” CERN, Geneva, Tech. Rep. CMS-CR-2013-379. arXiv:1311.4942, Oct. 2013. [Online]. Available: <https://cds.cern.ch/record/1626816>.
- [16] B. Isildak, “Measurement of the differential dijet production cross section in proton-proton collisions at $\sqrt{s} = 7$ TeV,” PhD thesis, Bogazici U., 2011. arXiv: 1308.6064 [hep-ex]. [Online]. Available: <https://inspirehep.net/record/1251416/files/arXiv:1308.6064.pdf>.
- [17] CMS Collaboration, “The CMS muon system in Run2: preparation, status and first results,” *PoS*, vol. EPS-HEP2015, p. 237, 2015. arXiv: 1510.05424 [physics.ins-det].
- [18] CMS Collaboration, “CMS technical design report for the level-1 trigger upgrade,” Tech. Rep. CERN-LHCC-2013-011. CMS-TDR-12, Jun. 2013. [Online]. Available: <https://cds.cern.ch/record/1556311>.
- [19] S. Van der Meer, “Calibration of the effective beam height in the ISR,” 1968.
- [20] CMS Collaboration, “Beams scan based absolute normalization of the CMS luminosity measurement. CMS 2010 luminosity determination,” 2011. [Online]. Available: <https://cds.cern.ch/record/1357856>.
- [21] CMS Collaboration, “CMS luminosity measurement for the 2015 data-taking period,” CERN, Geneva, Tech. Rep. CMS-PAS-LUM-15-001, 2017. [Online]. Available: <http://cds.cern.ch/record/2138682>.

- [22] CMS Collaboration Collaboration, “CMS luminosity measurements for the 2016 data taking period,” CERN, Geneva, Tech. Rep. CMS-PAS-LUM-17-001, 2017. [Online]. Available: <http://cds.cern.ch/record/2257069>.
- [23] CMS Collaboration, “Measurement of the properties of a Higgs boson in the four-lepton final state,” *Phys. Rev. D*, vol. 89, no. 9, p. 092007, 2014. DOI: 10.1103/PhysRevD.89.092007. arXiv: 1312.5353 [hep-ex].
- [24] CMS Collaboration, “Measurement of the inclusive W and Z production cross sections in pp collisions at $\sqrt{s} = 7$ TeV,” *JHEP*, vol. 10, p. 132, 2011. DOI: 10.1007/JHEP10(2011)132. arXiv: 1107.4789 [hep-ex].
- [25] J. Butterworth *et al.*, “PDF4LHC recommendations for LHC Run II,” *J. Phys.*, vol. G43, p. 023001, 2016. DOI: 10.1088/0954-3899/43/2/023001. arXiv: 1510.03865 [hep-ph].
- [26] Particle Data Group, C. Patrignani, *et al.*, “Review of particle physics,” *Chin. Phys. C*, vol. 40, no. 10, p. 100001, 2016. DOI: 10.1088/1674-1137/40/10/100001.
- [27] G. Bohm and G. Zech, *Introduction to statistics and data analysis for physicists*. DESY, 2010, ISBN: 9783935702416. [Online]. Available: <https://books.google.ch/books?id=aQBHcgAACAAJ>.
- [28] G. D’Agostini, “A multidimensional unfolding method based on bayes’ theorem,” *Nucl. Instrum. Meth.*, vol. A362, pp. 487–498, 1995. DOI: 10.1016/0168-9002(95)00274-X.
- [29] A. P. Dempster, N. M. Laird, and D. B. Rubin, “Maximum likelihood from incomplete data via the EM algorithm,” *J. R. Stat. Soc. B*, vol. 39, p. 1, 1977, ISSN: 00359246. [Online]. Available: <http://www.jstor.org/stable/2984875>.
- [30] L. B. Lucy, “An iterative technique for the rectification of observed distributions,” *Astron. J.*, vol. 79, p. 745, Jun. 1974. DOI: 10.1086/111605.
- [31] W. H. Richardson, “Bayesian-based iterative method of image restoration,” *J. Opt. Soc. Am.*, vol. 62, p. 55, Jan. 1972. DOI: 10.1364/JOSA.62.000055. [Online]. Available: <http://www.osapublishing.org/abstract.cfm?URI=josa-62-1-55>.
- [32] L. A. Shepp and Y. Vardi, “Maximum likelihood reconstruction for emission tomography,” *IEEE Transactions on Medical Imaging*, vol. 1, no. 2, p. 113, Oct. 1982, ISSN: 0278-0062. DOI: 10.1109/TMI.1982.4307558.

- [33] T. Adye, “Unfolding algorithms and tests using RooUnfold,” in *Proceedings, PHYSTAT 2011 Workshop on Statistical Issues Related to Discovery Claims in Search Experiments and Unfolding, CERN, Geneva, Switzerland 17-20 January 2011*, CERN, Geneva: CERN, 2011, p. 313. DOI: 10.5170/CERN-2011-006 . 313. arXiv: 1105.1160 [physics.data-an]. [Online]. Available: <https://inspirehep.net/record/898599/files/arXiv:1105.1160.pdf>.
- [34] Y. Vardi, “Empirical distributions in selection bias models,” *Ann. Statist.*, vol. 13, p. 178, Mar. 1985. DOI: 10.1214/aos/1176346585. [Online]. Available: <http://dx.doi.org/10.1214/aos/1176346585>.
- [35] F. Pedregosa, G. Varoquaux, A. Gramfort, V. Michel, B. Thirion, O. Grisel, M. Blondel, P. Prettenhofer, R. Weiss, V. Dubourg, J. Vanderplas, A. Passos, D. Cournapeau, M. Brucher, M. Perrot, and E. Duchesnay, “Scikit-learn: Machine learning in Python,” *J. Mach. Learn. Res.*, vol. 12, p. 2825, 2011.
- [36] D. Rainwater, R. Szalapski, and D. Zeppenfeld, “Probing color-singlet exchange in $Z + 2$ -jet events at the CERN LHC,” *Phys. Rev. D*, vol. 54, p. 6680, 11 Dec. 1996. DOI: 10.1103/PhysRevD.54.6680. [Online]. Available: <https://link.aps.org/doi/10.1103/PhysRevD.54.6680>.